Experimental Mechanics (2024) 64:1021–1036
https://doi.org/10.1007/s11340-024-01074-w

RESEARCH PAPER

Experiments on Low–Cycle Ductile Damage and Failure Under Biaxial Loading Conditions

S. Gerke[1] · **Z. Wei**[1] · **M. Brünig**[1]

Received: 2 August 2023 / Accepted: 17 April 2024 / Published online: 20 May 2024
© The Author(s) 2024

Abstract

Background The damage and failure behavior of ductile metals depends on the stress state as well as on the loading history. Biaxial experiments with suitable specimens can be used to targeted generate different loading conditions, thus allowing the investigation of a wide variety of load cycles with different stress states.

Objective In the biaxial experiments with the newly presented HC-specimen cyclic shear loads are superimposed by various constant compressive and tensile loads. Buckling during compressive loading in both axes is avoided by an additional newly introduced downholder.

Methods The strain fields at the surfaces of the biaxial specimens are evaluated by digital image correlation (DIC), and after failure the corresponding fracture surfaces are analyzed by scanning electron microscopy (SEM). Associated numerical simulations employing the presented material model provide information on the current stress states.

Results The introduced downholder successfully prevents buckling during compressive loading. The strain fields detect a clear influence of the shear direction and a tensile superposition of the cyclic shear load leads to more brittle and a compressive superposition to more ductile behavior. The accompanying numerical calculations reveal the associated, different stress states.

Conclusions The new experimental program with biaxially loaded specimens for the investigation of damage and failure behavior under cyclic loading enables the targeted examination of a wide variety of load cycles and is thus suitable for the comprehensive analysis of these phenomena.

Keywords Low-cycle ductile damage · Biaxial cyclic experiments · Compressive loading · Downholder

Introduction

Sheets of steel or aluminum alloys are exceptionally important in many engineering applications. In this context, they are frequently used as raw materials for the production of safety-relevant components. The production of these structural parts is often carried out by multi-stage cold forming, during which cyclic loads can also occur as a result of load reversal. Thus, non-propor- tional, in certain cases, cyclic load scenarios also occur in the individual material points. In this process, larger inelastic deformations are frequently present in addition to reversible elastic ones. These permanent deformations are initially plastic and, as the deformation progresses, first significant micro-defects, i.e., damage, appear. Especially during the manufacturing process, these degradation mechanisms must be controlled to avoid initial macro-cracks. The damage caused during manufacturing is also essential for the subsequent use of the components.

In order to make an accurate prediction of the material behavior by means of numerical simulations, an adequate and efficient phenomenological description is essential. In this context, it has to be taken into account that in ductile metals mostly larger plastic deformations occur before material degradation, i.e. damage, has to be considered [1]. Thus, special attention must be given initially to the description of plastic material behavior under compressive and tensile

✉ S. Gerke
steffen.gerke@unibw.de

Z. Wei
zhichao.wei@unibw.de

M. Brünig
michael.bruenig@unibw.de

[1] Institut für Mechanik und Statik, Universität der Bundeswehr München, Werner-Heisenberg-Weg 39, D-85577 Neubiberg, Germany

stresses, as well as non-proportional and cyclic loading. On the one hand, it is often observed that plastic flow begins at higher stresses in the compressive region than in the tensile region. This effect is known as the strength-differential (SD) effect and occurs in metals [2–4]. On the other hand, in the case of non-proportional load increase and especially in the case of load reversal (cyclic loading), a description by using isotropic hardening might not be possible, so that using mixed (isotropic and kinematic) hardening is often employed [5–8].

As deformation progresses, significant damage processes begin at a specific point. The onset as well as the formation of these damage processes are significantly influenced by two factors: (i) the stress state in the material point and (ii) the loading history. Thus, tensile dominant stress states characterized by positive stress triaxialities lead to the formation, growth and coalescence of micro-pores, whereas micro-cracks form in shear stress states with stress triaxialities around zero. The transition between these two states is fluent, see e.g. [9, 10]. Biaxial experiments with different non-proportional load paths [11, 12] clearly demonstrated the dependence of the damage mechanisms on the loading history. In this context, loading scenarios with cyclic load reversal can be considered as a special non-proportional loading case where failure occurs after ductile damage evolution. If the number of cycles remains very low, a clear distinction from fatigue failure can be made by observing the fracture surfaces [13].

The specimens for sheet metals presented in the literature are often designed in such a way that exactly one stress distribution can be investigated with one specimen geometry, see [12] for a detailed discussion. In addition, the standard testing machine applied is tension loaded only to avoid buckling. Thus, dog-bone-shape specimens without notch show a stress triaxiality of 1/3 under tensile loading, whereas compressive loadings of the standardized geometries are not intended. However, if the homogeneous region is made more compact and the testing machine is aligned very accurately, compressive loads leading to moderate plastic deformations can be applied with caution [13]. If notches are introduced to the sides of dog-bone-shape specimens, the stress triaxiality in the center of the specimen increases as the notch radius decreases [10, 14, 15]. In addition, it can be observed that significant stress gradients are present in contrast to the dog-bone-shape specimen with a homogeneous central region. Shear stress states can be generated on a standard testing machine using special specimen geometries, see e.g. [10, 16], while it is even possible to achieve cyclic shear scenarios using special geometries under successively applied tensile loads [17]. It has also been possible to successfully test double shear specimens under cyclic loading with very accurate alignment of the testing machine [13]. Another possibility to investigate cyclic shear loads on plates is provided by a circular notched torsion test specimen [18] as well as a previous version with two connectors [19]. For both test specimens, however, a special testing machine is mandatory to perform the experiments. The frequently discussed butterfly specimen [20, 21] allows the generation of a wide range of stress states by applying displacements in two directions by a special testing machine. This geometry can be considered as a further development of the Arcan specimen [22], where the shaping of the region of interest forces larger strain gradients, allowing locally occurring cracking before failure of the whole specimen. Overall, conducting cyclic tests to investigate ductile damage presents an experimental challenge, as significant inelastic deformations must be achieved under both tensile and compressive loading, and this can lead to stability problems in compression, which often must be compensated by structural components.

The execution of experiments under compressive loading especially for sheet metal, where mainly constructive measures have to be taken to avoid buckling and the influence of boundary effects due to friction have to be solved is a big challenge. For more solid materials, it is possible to produce cylinders with a certain thickness to height ratio, as described in ASTM Standard E9-09, and to compressively load them in cylinder direction. Even in this experiment, barrel shaped deformations occur due to friction at the load application surfaces. Sheet materials can be tested in a similar way under compressive load. For this purpose, coin-shaped cutouts are manufactured from the sheet and stacked to form a cylinder, which is then tested in the so-called stacked compression test [23–25]. Here, however, the material properties are determined in sheet thickness direction. To determine the material properties in the sheet plane, dog-bone shaped specimens are used, which are held laterally during the experiment and friction must be reduced by a lubricant [26–28]. However, this lateral support along with lubricant makes it difficult to use optical measurement systems such as digital image correlation. Also, it has been suggested to glue several thin samples to reduce the stability problem [28]. In this context, it can also be noted that with biaxial specimens, the risk of buckling is lower, as long as one axis is tensile loaded [29].

Biaxial testing machines offer the possibility of applying a wide range of loading conditions, whereby the loading is generally applied symmetrically on the axes in order to avoid transverse loads on the test cylinders. The geometry of the test specimens and the focus of the test series are of central importance in these experiments. If the focus is on the characterization of the yield surface as well as its evolution at moderate plastic deformations, a big variety of test specimens has been presented, see e.g. [30] for an overview, but all of them are characterized by a central region in which a stress and strain state as homogeneous as possible should be generated. However, this homogeneity can only

approximately be achieved for small to moderate strains, and as deformation progresses, unintended localization starts to occur, which makes an evaluation of the experiment based on homogeneous stress and strain fields impossible [31]. Thus, experimental investigation of damage and failure behavior with this type of test specimen appears to be difficult.

The dependence of the damage and failure behavior on the load path could be clearly demonstrated, for example, by experiments on the microscale using *in situ* X-ray tomography and *in situ* scanning electron microscopy (SEM) [32] under load reversal. This influence could also be underlined with tube-shaped specimens since they allow tensile or compressive loads, torsion and internal pressure [33, 34]. Unfortunately, such test specimens cannot be fabricated from sheet materials of moderate thickness. For these materials, two-step tensile tests are often used to investigate the load path dependence of the forming limit curves [35, 36], although only tensile loads are possible in this case and complete unloading is unavoidable before the second fabrication and loading step. Consequently, the investigation of ductile damage and failure behavior under loads with few cycles at a wide range of stress states is necessary.

In this context, the new biaxial H and X0-specimens were introduced to investigate the ductile damage and failure behavior of sheets [31]. These specimens could be successfully used under both proportional and non-proportional loads and associated numerical investigations covering a wide range of stress conditions [11, 12]. Also, one-dimensional cyclic loading in tension/compression as well as in shear could be successfully investigated experimentally as well as numerically [13]. In this paper, we follow up on this experimental and numerical work by evaluating a series of biaxial experiments and associated elastic–plastic simulations under cyclic loads with three half cycles to failure. For this purpose, the H-specimen is adapted for cyclic shear loading. In the experimental series, specified compressive and tensile load levels are set in one axis and cyclic loading causing shear stress states is applied in the second axis. Associated proportional experiments serve as reference. A new downholder is introduced to prevent buckling. Consequently, the present paper is organized as follows: the next section gives a brief overview of the material model proposed by [13] and in "Material" section details on the applied aluminum alloy EN AW 6082 (AlSiMgMn) are outlined and a full set of material parameters is given. In "Experimental Procedure" section the experimental realization is described in detail and corresponding numerical aspects are addressed. The main part of the paper focuses on biaxial experiments under proportional and cyclic loading with the new HC-specimen and the experimental and numerical results are discussed. In continuation the results of the new experimental series are related to one-dimensionally loaded experiments presented in [13]. Finally, the main results are concluded and perspectives on future work are given.

Constitutive Modeling

The phenomenological continuum damage model is based on the kinematic separation of elastic, plastic and damaging material behavior [37]. In [13] special focus has been given on the plastic material behavior and the model has been extended to reflect the SD effect and mixed hardening to describe the plastic material behavior under reversed loading conditions. The accompanying numerical simulations have been realized based on this elastic–plastic model and consequently a brief summery is given here. In addition, the aim of the new biaxial experiments discussed in detail within this paper is the determination of the ductile damage and fracture behavior under cyclic loading conditions. Consequently, an outlook on the damage modeling is given.

The investigated material is characterized by higher yield stresses under compressive loads than under tensile loads [13]. This phenomenon is known as the SD effect [38] and can be described by the hydrostatic stress-dependent Drucker-Prager type yield condition

$$f^{\mathrm{pl}} = \sqrt{\frac{1}{2}\mathrm{dev}\left(\bar{\mathbf{T}}-\bar{\boldsymbol{\alpha}}\right)\cdot\mathrm{dev}\left(\bar{\mathbf{T}}-\bar{\boldsymbol{\alpha}}\right)} + \bar{c}\left(\frac{a}{\bar{c}}\mathrm{tr}\left(\bar{\mathbf{T}}-\bar{\boldsymbol{\alpha}}\right)-1\right)=0\,, \tag{1}$$

where $\bar{\mathbf{T}}$ depicts the effective Kirchhoff stress tensor and the equivalent yield stress

$$\bar{c} = c_0 + Q_1(1-e^{-p_1\gamma}) + Q_2\xi(1-e^{-p_2\gamma}) \tag{2}$$

represented by an extended Voce hardening law for isotropic hardening. In equation (2) γ denotes the equivalent plastic strain, ξ an additional function variable, Q_1, Q_2 the hardening moduli and p_1, p_2 the hardening exponents. Furthermore, in equation (1) the hydrostatic stress coefficient $a/\bar{c}$ can be assumed to be constant [13, 37]. To describe properly reverse loading conditions the effective back stress tensor $\bar{\boldsymbol{\alpha}}$ for kinematic hardening is introduced. In this context the modified Chaboche kinematic hardening model is used for the rate of the back stress tensor

$$\dot{\bar{\boldsymbol{\alpha}}} = \dot{\bar{\boldsymbol{\alpha}}}_1 + \dot{\bar{\boldsymbol{\alpha}}}_2 + \dot{\bar{\boldsymbol{\alpha}}}_3 \tag{3}$$

with

$$\begin{aligned}\dot{\bar{\boldsymbol{\alpha}}}_1 &= b_1\chi\dot{\bar{\mathbf{H}}}^{\mathrm{pl}} - b_2\chi\dot{\gamma}\bar{\boldsymbol{\alpha}}_1\,,\\ \dot{\bar{\boldsymbol{\alpha}}}_2 &= b_3\dot{\bar{\mathbf{H}}}^{\mathrm{pl}} - b_4\dot{\gamma}\bar{\boldsymbol{\alpha}}_2 \quad \text{and}\\ \dot{\bar{\boldsymbol{\alpha}}}_3 &= b_5\dot{\bar{\mathbf{H}}}^{\mathrm{pl}} - (1-\cos^2\theta)b_6\dot{\gamma}\bar{\boldsymbol{\alpha}}_3\,.\end{aligned} \tag{4}$$

Here $\dot{\mathbf{H}}^{\mathrm{pl}}$ represents the plastic strain rate tensor, χ an additional function variable, θ an additional angle parameter and $b_1 \ldots b_6$ the hardening moduli. The ratio between the equivalent stress rate $\dot{c}$ and the equivalent back stress rate $\dot{\alpha}$ is defined by the scalar parameter ρ as

$$\dot{\bar{\sigma}} = \rho\dot{c} + (1-\rho)\dot{\alpha}\,, \tag{5}$$

and consequently the hardening rate $\dot{\bar{\sigma}}$ is split and mixed hardening is enabled.

Damage material behavior is modeled in a similar way. The onset of damage is specified by the damage criterion

$$f^{\mathrm{da}} = \alpha I_1 + \beta\sqrt{J_2} - \tilde{\sigma} = 0 \tag{6}$$

where $\tilde{\sigma}$ is the equivalent damage stress, I_1 the first stress invariant and J_2 the second deviatoric stress invariant. In addition the damage strain strain rate is given by

$$\dot{\mathbf{H}}^{\mathrm{da}} = \dot{\mu}(\tilde{\alpha}\frac{1}{\sqrt{3}}\mathbf{1} + \tilde{\beta}\tilde{\mathbf{N}}) \tag{7}$$

where $\tilde{\mathbf{N}}$ is the transformed normalized deviatoric stress direction and $\dot{\mu}$ represents the equivalent damage strain rate whereas the modeled damage material behavior is strongly influenced by the stress-state-dependent variables α, β, $\tilde{\alpha}$, and $\tilde{\beta}$ [39]. In this context the stress state is generally characterized by the triaxiality

$$\eta = \frac{\sigma_{\mathrm{m}}}{\sigma_{\mathrm{eq}}} = \frac{I_1}{3\sqrt{3J_2}} \tag{8}$$

defined by ratio of the mean stress σ_{m} and the von Mises equivalent stress σ_{eq} and the Lode parameter

$$\omega = \frac{2T_2 - T_1 - T_3}{T_1 - T_3} \quad \text{with} \quad T_1 \geq T_2 \geq T_3 \tag{9}$$

with principal stresses T_i. A detailed discussion of the material modeling can be found in [13]. Furthermore, the model has been implemented as user defined subroutine into Ansys 18 and the numerical results presented within this paper have been realized with the elastic–plastic model. Moreover, the identified material parameters have been verified under different monotonic and complex biaxial cyclic loading conditions [40–42]. The numerical results show good agreement with the experimental ones. The focus of this publication is on the experimental aspects of the test series, whereby an interpretation of the results is considerably facilitated with the assistance of the stress state, which can only be determined numerically based on the proposed theoretical framework.

Table 1 The chemical composition of EN-AW 6082-T6 (AlSiMgMn) in weight percent

Si	Fe	Cu	Mn	others
0.9	0.37	0.09	0.47	0.04
Cr	**Zn**	**Ti**	**Mg**	**Al**
0.02	0.09	0.03	0.7	to balance

Material

The aluminum alloy EN AW-6082 T6 has been chosen with a sheet thickness of 4 mm. It belongs to the high-strength aluminum-magnesium-silicon (AlMgSi) alloys and has good welding and machining properties. Common applications are in automotive and aircraft production as well as shipbuilding and pump technology. The chemical composition is given in Table 1 and has been determined by cast analysis of the supplied material.

Figure 1 displays the load–displacement curve (EXP) which has been generated in tension experiments with dog-bone-shape TC-specimens of 16 mm^2 cross section. The initial distance of measuring points is 9 mm, see [13]. A corresponding elastic–plastic numerical simulation with the parameters given in Table 2, including the elastic ones (Young's modulus E and the Poisson's ratio ν), has been realized and the corresponding graph is displayed in Fig. 1 (SIM). The parameters of the modified Chaboche kinematic hardening model (equation (4)) and the proportion parameter ρ (equation (5)) for mixed hardening have been determined by one-axis-loaded cyclic experiments. Details on material

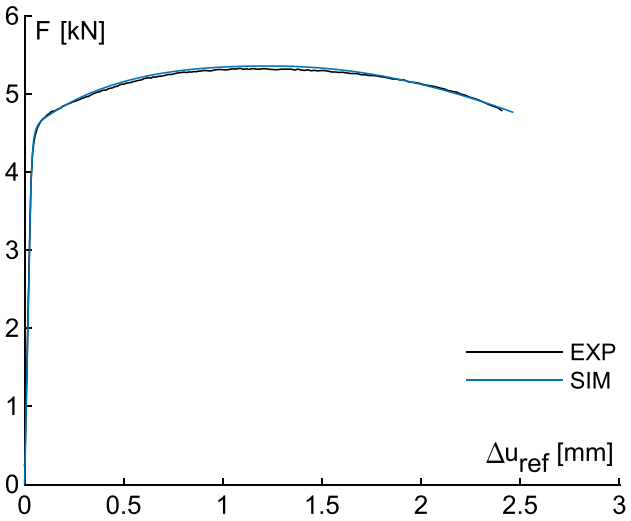

Fig. 1 Experimental and numerical force - displacement curve for the uniaxial tension test

Table 2 Material parameters

E[MPa]	ν[−]	c_0[MPa]	Q_1[MPa]	Q_2[MPa]
67500	0.3	139	74.93	21.31
p_1[−]	p_2[−]	b_1[MPa]	b_2[−]	b_3[MPa]
8.96	676.01	12250	350	895
b_4[−]	b_5[MPa]	b_6[−]	$a/\bar{c}$[TPa^{-1}]	ρ[−]
15	155	7.5	32	0.405

parameter identification including specimen geometries and experimental program can be found in [8, 13].

Experimental Procedure

Biaxial experiments enable the specific generation of a wide variety of stress and strain states in the specimens region of interest through the targeted application of loads or displacements. In biaxial testing transverse loads on the clamping jaws are generally not intended and may lead to damage of the testing device. Furthermore, these transversal loads usually cannot be measured and consequently the application of symmetrical loads in combination with symmetrical test specimens is essential [31]. Based on these considerations, the loads of the two cylinders in one axis have to coincide and only different load ratios between the two axes are possible, which are, however, coupled by the geometry of the specimen. Under these conditions, the original geometry of the H-specimen was presented [31]. In this original design, primarily tensile loading was intended and additionally the region of interest, which is evaluated by digital image correlation, was kept small to explore the quality of the measurements best possible [31]. Compressive loads are generally a challenge due to stability problems and the execution can only be realized in certain limits without additional precautions. However, if the displacements out of the loading plane are suppressed, a large number of loading conditions in tension and compression range is possible in a biaxial test setup. In addition, if suitable specimens are used cyclic loading can be applied in a controlled manner.

The HC-specimen presented in Fig. 2 is based on the design of the H-specimen [29, 31] whereby the essential basic ideas could be transferred. These can be summarized as follows:

- Well accessible connection between applied load and resulting stress state in the area of interest. Loading in axis 2 produces mainly tensile or compressive stresses, depending on the direction, and tensile loads in axis 1 results mainly into shear stresses in the notch region.
- The specimen can be used under a wide range of stress conditions, which can be specifically adjusted. Dominant shear stresses can be superimposed on tensile or compressive stresses, and dominant tensile or compressive stresses can also be superimposed with shear stresses.
- The specimen is plane-symmetrical with respect to the planes defined by the load axes and the normal of the sheet plane, as well as with respect to the sheet plane itself.
- Notches in thickness direction determine the localization and thus also the area where damage and failure occurs.
- The area of interest of the specimen is compact and thus well evaluable by means of digital image correlation (DIC).
- The specimens can be manufactured by drilling and milling in order to keep the manufacturing costs within acceptable limits and to minimize the influence of the manufacturing process on the machined parts.

The H-specimen was successfully used for a wide range of stress conditions under proportional [29, 31] and non-proportional loading [11, 43]. Compressive loads with the H-specimen are limited by stability issues (buckling), i.e. significant displacements normal to the sheet plane. In this context the maximum compressive load is related to the load of the second axis whereat higher tensile loads suppress buckling. Furthermore, in the design of the H-specimen no compressive loading was intended since very similar shear stress states can be achieved under tensile loading avoiding stability problems. Consequently, for reverse shear loading, a modification of the specimen design has to be realized. In addition, to achieve higher pressure loads without significant displacements out of the sheet plane, constructive measures have to be taken.

The here newly presented HC-specimen is characterized by four notched regions arranged parallel to axis 1 and separated by a central opening, see Fig. 2(a). The notch depth here is 1 mm, reducing the sheet thickness (4 mm) in these areas to 2 mm (Fig. 2(d)). Consequently, each notched section has a minimum cross section of 12 mm^2. The notches pass into elongated holes with a 3 mm radius in the sheet plane (Fig. 2(c)) and by 8 mm spacing between the connectors (Fig. 2(b)), compressive loads in axis 1 become possible as well. Consequently, the new geometry allows tensile and compressive loading in both axis and tension compression cycles are possible in both axis.

The biaxial experiments have been conducted on the horizontally arranged electro-mechanical device LFM-BIAX 20 kN (produced by Walter & Bai, Switzerland) under quasi-static loading conditions with a constant leading machine velocity of 0.04 $^{\mathrm{mm}}/_{\mathrm{min}}$. The displacements and strains of the specimen surfaces have been monitored by a digital image correlation (DIC) system provided by Dantec/Limess with corresponding evaluation software Istra4D. The force signals $F_{i,j}$ and the machine displacements $u^{\mathrm{M}}_{i,j}$ of

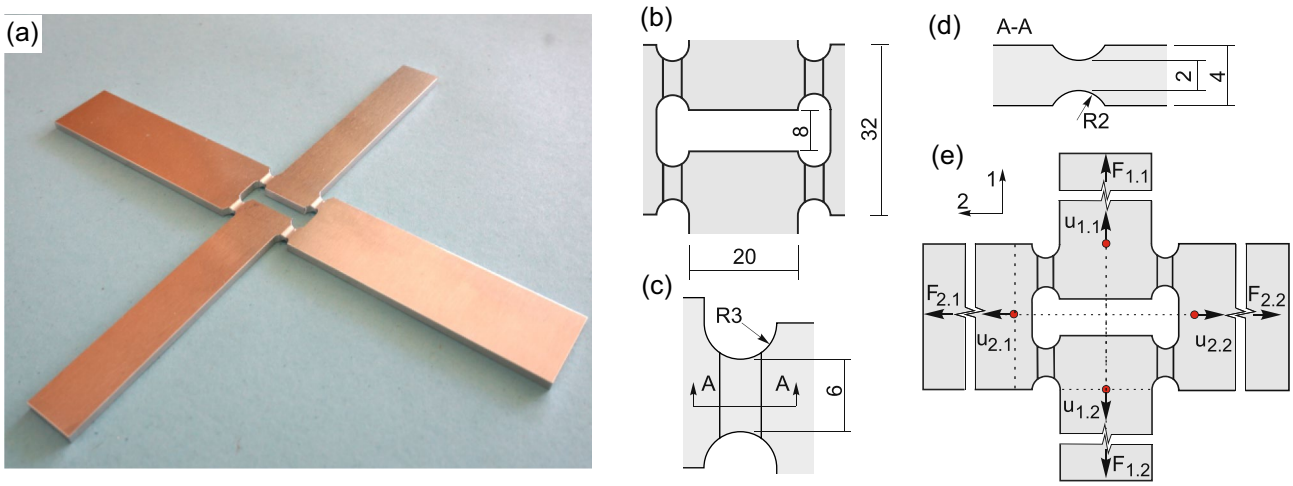

Fig. 2 Biaxially cyclic loaded HC-specimen: (**a**) isometric photo of the HC-specimen, (**b**) central part, (**c**) detail of the notched part, (**d**) cross section A-A of notched part and (**e**) notation (all dimensions in mm)

the four cylinders (see Fig. 2(e)) have been transmitted to the DIC system where they were stored with the associated image data. The DIC setup consists of two 6 MPx cameras equipped with 75 mm lenses, two monitoring the upper of the specimen, see Fig 3(a). The cameras have been calibrated into a common coordinate system with a 40 mm calibration target provided by Limess/Dantec. The specimens were prepared shortly before the experiment with white acrylic lacquer, and in continuation, a black speckle pattern was sprayed on with a graphite-based coating and a intermediate speckle diameter of approximately 3 to 5 Px. The average camera resolution at the center of the specimen is approximately 56 $^{\mathrm{Px}}/_{\mathrm{mm}}$, and the subset (facet) size was selected to 33 Px with a grid spacing (overlap) of 11 Px, i.e., a step size of $^{1}/_{3}$. The region of interest (ROI) has been approximately 2500 Px by 2000 Px and for the presentation of the results a representative cut out containing all four notches has been chosen. With this setup for one notched region (6 mm by 3.46 mm), see Fig. 2(c) a resolution of 14 to 8 facets could be achieved. Consequently, the parameters for the DIC setup and evaluation were chosen in accordance with the manufacturer's recommendations as well as the recommendations of good practice [44]. Data sets have been saved with a frequency of 1 Hz. The nominal relative displacement measures are given by the sum of the displacements of the red dots indicated in Fig. 2(e)

$$\Delta u_{\mathrm{ref.i}} = u_{i.1} + u_{i.2}\,. \tag{10}$$

The initial distance between measuring points is 32 mm in 1-direction and 38 mm in 2-direction. At this point it can be noted that the relationship between the machine displacements $u^{\mathrm{M}}_{i.j}$ and the nominal displacements $u_{i.j}$ is nonlinear and depends on the load case. Furthermore, the mean forces

$$F_i = \frac{F_{i.1} + F_{i.2}}{2} \tag{11}$$

are introduced whereat differences between $F_{i.1}$ and $F_{i.2}$ are generally negligible.

In order to limit the displacements perpendicular to the sheet plane, the new downholder (Fig. 4) was developed and manufactured in cooperation with Walter & Bai. The limited installation space between the clamping heads, the use of a two-sided DIC system and the possibility of precise alignment, especially in height (Fig. 3(b)), had to be taken into account. The solid base can be accurately aligned on the base plate of the machine by means of swivel brackets. The height of the lower roller bearings is then adjusted by means of rotary controls and checked both visually and acoustically after installation of the cross-check. After installation of the biaxial specimen, the upper part of the downholder is mounted and preloaded via springs which are tensioned by rotary controls, Fig. 3(c). The use of rollers as an additional support keeps the friction effects to a minimum. By means of this hold-down device, the compressive loads of up to 6 kN desired in the series of tests presented here could be applied without significant displacements out of the sheet plane being observed.

Experiments and associated numerical simulations under a big variety of loading conditions have been realized with the H-specimen. Based on these experiences the material behavior over a wide range of controlled generated stress conditions has been analyzed including damage and fracture [29]. In addition, tests with one load change showed that the stress state in the damage and failure regions (notches) could also be specifically altered in a targeted manner by the load change [11]. Based on this

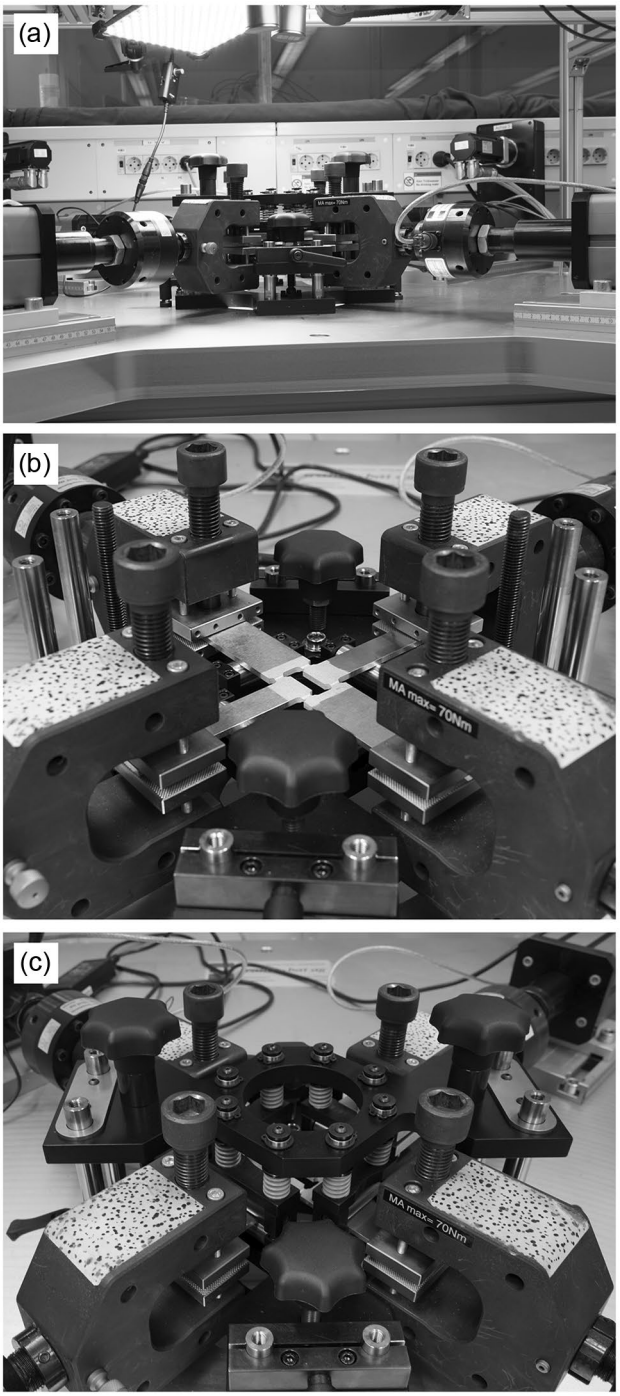

Fig. 3 Biaxial test machine and digital image correlation setup including downholder: (**a**) lighting system and DIC cameras, (**b**) clamping and open downholder, (**c**) closed downholder

experience, it seems possible to experimentally realize cyclic loading sequences with a modified H-specimen and thus to specifically investigate the damage and failure behavior depending on the loading history and the stress state. With this approach a wide range of cyclic loading conditions and consequently of stress states can be realized.



Fig. 4 Downholder

In this context, a cycle is to be understood as a phase of the test until the initial loading condition is reached again and a new cycle is applied. As stated above, the HC-specimen allows alternating loads in axis 1 (Fig. 2(e)) resulting in alternating shear stresses. Furthermore, these can be selectively superimposed by tensile or compressive loads from axis 2. Thus, it is possible to investigate cyclic shear loads superimposed by tension or compression with the HC-specimen and the first here presented test series could be designed: Under constant load in axis 2, applied in advance and then held during the test, a cyclic load is applied in axis 1, with loading to failure at the last tensile load. Five load levels of 0, 3, −3, 6 and −6 kN were selected for the preload (axis 2) and failure was induced after 1.5 cycles (axis 1). In addition, experiments with the same preload levels in axis 2 and monotonically increased machine paths in axis 1 are performed for comparison and to determine the points of load reversal of the cyclic experiments.

In addition to the symmetry properties of the specimen, a largely symmetrical test procedure is essential for the success of biaxial experiments with pre-defined loading. For this purpose, a predominantly displacement-controlled test routine is used, whereby small differences in the forces of cylinders of the same axis cannot be completely avoided. In this test routine, one cylinder is always conducting the axis and the scond cylinder in each axis is following. Cylinder 2.1 is leading during preloading and cylinder 1.1 during the subsequent cyclic loading, see Fig. 2(e). An overview of the test routine is given in conjunction with Fig. 2(e). For preloading the four cylinders are controlled as follows:

- The machine displacement $u^{M}_{2.1}$ in cylinder 2.1 is increased continuously. For the positive preloadings 3 and 6 kN in positive (tension) direction, for the negative preloadings −3 and −6 kN in negative (compression) direction and for zero preloading no displacement is applied.
- The same machine displacement $u^{M}_{2.2}$ is applied to cylinder 2.2, i.e. opposite on the same axis.
- During this preloading process, the load in cylinder 1.1 is kept constant zero. However, this might result in small machine displacements $u^{M}_{1.1}$.
- The same machine displacement of cylinder 1.1 is applied to cylinder 1.2 in a displacement controlled manner as $u^{M}_{1.2}$.

Thus, three cylinders are displacement-controlled and only cylinder 1.1 is load-controlled. For subsequent cyclic loading the following routine is applied within each half cycle:

- The machine displacement $u^{M}_{1.1}$ in cylinder 1.1 is increased continuously in positive (tension) direction in half cycle 1 and 3 and in negative (compression) direction in half cycle 2.
- The same machine displacement $u^{M}_{1.2}$ is applied to cylinder 1.2, i.e. opposite on the same axis.
- During this process, the load in cylinder 2.1 is kept constant at the preloading level. This generally results not negligible machine displacements $u^{M}_{2.1}$.
- The same machine displacement of cylinder 2.1 is applied to cylinder 2.2 in a displacement controlled manner as $u^{M}_{2.2}$.

Consequently, the routines during preloading and cyclic loading are very similar whereat after preload the leading cylinder is changed from axis 2 to axis 1. This procedure also ensures that the center of the specimen remains almost displacement-free during the test. It is also important to note that the points of load reversal (LR) under cyclic loading must be determined in advance, based on tests with monotonic loading. For this purpose, suitable machine displacements $u^{M}_{1.1}$ are determined.

After the experiments, the fracture surfaces of selected specimens were analyzed by scanning electron microscopy. The ZEISS EVO 15 with lanthanum hexaboride electron emitter (LaB6) and Everhart-Thornley (ET) detector were used in the present work. Imaging was performed in high vacuum, with a working distance of about 11 mm, electron beam diameter (spot-size) of 300 nm and accelerating voltage of 20 kV. This approach allows the assessment of the damage and failure mechanism based on the texture of the surfaces.

In order to make the stress state in the notch regions accessible, it is necessary to perform numerical simulations. For this purpose, the material law presented in "Constitutive Modeling" section was connected to Ansys 18 via the user interface and used for the calculations. Figure 5(a) displays the mesh in the notch region generated with solid185 elements. In total, the mesh of a quarter specimen considering symmetry conditions and shortening the connector arms consists of 22502 elements, whereby a significant mesh refinement was applied in the notch region in order to reproduce stress gradients realistically. Figure 5(b) shows a cross section through the notch in detail and the area chosen for stress reproduction has been marked in red.

Overally, the experimental and numerical setup described here enables the targeted investigation of the ductile damage behavior of sheet metal under cyclic loading. This is made possible in particular by the newly presented HC-specimens and the newly designed test routine.

Results

In the context of damage behavior of ductile metals the stress state is frequently characterized by the stress triaxiality η (equation (8)) and the Lode parameter ω (equation (9)). Figure 6 displays both quantities at the cross section given in Fig. 5(b) under different preloads for monotonic loading shortly before fracture occurrence. If axis 2 is maintained unloaded (0) and only axis 1 is loaded, a stress triaxiality with values around zero is obtained and the Lode parameter is in the small positive range close to zero. Thus, nearly a shear stress state ($\eta = 0$ and $\omega = 0$) is present. If a tensile load is applied to axis 2 ((3) and (6)), triaxiality values of around 0.2 (3) and 0.4 (6) are obtained and the values of the Lode parameter are in the range of −0.2 (3) and −0.55 (6) respectively. If, on the other hand, a pressure preload is applied ((−3) and (−6)), lower values of around −0.12 (−3) and −0.26 (−6) are obtained for the stress triaxiality and the values for the Lode parameter show higher values of about 0.2 (−3) and 0.4 (−6). Thus, the desired influence of preloading is clearly visible. Overall, the stress distributions

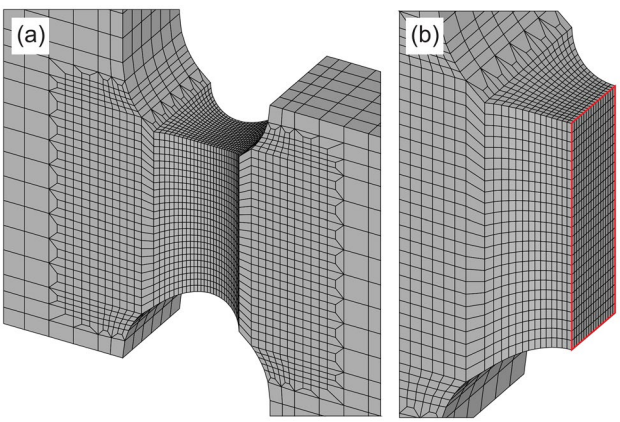

Fig. 5 (**a**) Mesh of notched part (**b**) Cross section for stress evaluation

in the center of the notch are homogeneous, with detectable gradients only at the slotted holes, see Fig. 6.

The global behavior of the specimens under monotonic and cyclic loading can be well assessed by the loads on the two axes F_i (equation (11)) and the nominal displacements $\Delta u_{\mathrm{ref}.i}$ (equation (10)). Figure 7 shows corresponding curves of the experiments with monotonic load increase and Fig. 8 under cyclic loading. For the graphical representation (Figs. 7 and 8), each load case was assigned by one color, which will be used consistently in the following. The experiments with cyclic loading are shown in full color and the proportional experiments in the corresponding lighter colors.

The preloads in axis 2 are applied up to the predefined load levels (after preloading (AP)) causing a relative displacement in axis 2 $\Delta u_{\mathrm{ref}.2}$ before load starts in axis 1. During the course of the experiment, this load level is maintained, i.e. the force is held and the displacements are readjusted accordingly. Tensile preloading (3kN and 6kN) results in small positive and compressive preloading in small negative relative displacements $\Delta u_{\mathrm{ref}.2}$, see Table 3. After reaching the preload level in axis 2, the displacements in axis 1 are monotonically increased until failure, whereas the maximum relative displacement $\Delta u_{\mathrm{ref}.1}$ reached strongly depends on the preload, see Fig. 7. Under 6 kN preload $\Delta u_{\mathrm{ref}.1} = 1.4$ mm, under 3kN $\Delta u_{\mathrm{ref}.1} = 1.9$ mm, without preload already $u_{\mathrm{ref}.1} = 2.3$ mm and under the pressure preloads −3 kN and −6 kN, respectively, $u_{\mathrm{ref}.1} = 3.0$ mm are reached. In axis 2 (preload), due to load control, i.e. holding the preload, further relative displacements $\Delta u_{\mathrm{ref}.2}$, in some cases significant, are observed, being positive for positive preloads and no preloads, and negative for compressive preloads and the relative displacements at fracture (FP) are given in Table 3. However, an influence of the preload on the elastic material behavior is not evident for the tests with monotonic load increase, since all curves show a similar slope in this region,

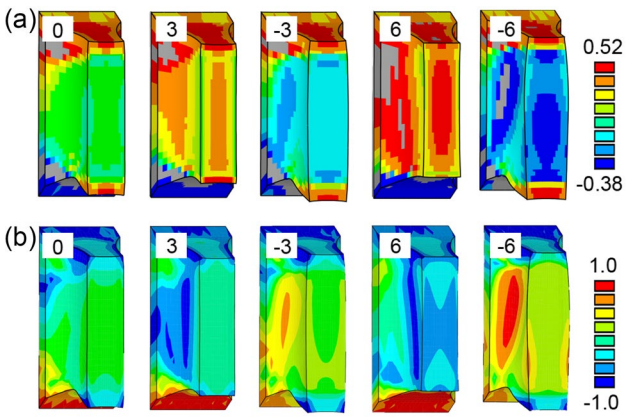

Fig. 6 (**a**) Triaxiality η and (**b**) Lode parameter ω in the notched cross section, respectively without preload (0) as well as for preloads 3, −3, 6 and −6 kN

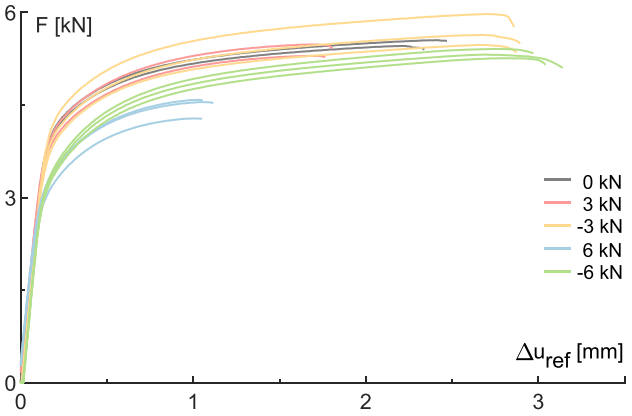

Fig. 7 The experimental force-displacement curves for monotonic loadings

see Fig. 7. The influence of the preload on the onset of platic yielding is however recognizable, under preloads of −6 kN and 6 kN an earlier transition into the elastic–plastic region is evident. All experiments were performed three times, if there was good agreement after one repetition, only two tests were carried out, and show excellent repeatability and the corresponding curves are shown in Fig. 7.

A major challenge in conducting cyclic tests under ductile material damage is the determination of the points in the loading process at which the load reversal is performed. These points must be determined before the test in terms of machine displacements, whereby the relationship between machine displacements ($\Delta u^{\mathrm{M}}_{i,j}$) and nominal displacements Δu_{i} is nonlinear and depends on the preload. A wide range is possible when defining the load reversal points, although the maximum value is limited by anticipatory failure. In the series of experiments presented here, the point of the first (RP1, ○) and the second load reversal (RP2, □) were determined based on the experiments with monotonic load increase (Fig. 7) and preliminary tests so that the load reversal takes place as late as possible without failure occurring during the first two half cycles. Failure should not occur until the third half cycle and the failure point is marked FP, (△). The symbols (○, □ and △) introduced here are used in the following figures in the color of the load case.

The cyclic biaxial experiments with different preloads were repeated three times each, if there was good agreement after one repetition, only two tests were carried out, and the obtained curves are shown in Fig. 8. Again, there is good repeatability. The preloads as well as the three applied half cycles to failure can be seen well for all load cases. Without preloading (a), the largest relative displacement of $\Delta u_{\mathrm{ref}.1} = 1.0$ mm up to RP1 could be applied in the first half cycle and also the displacement up to RP2 of 1.8 mm ($\Delta u_{\mathrm{ref}.1} = -0.8$ mm is maximum compared to the cyclic tests with preloading (b–e), see also (f). Under tensile preload (3kN

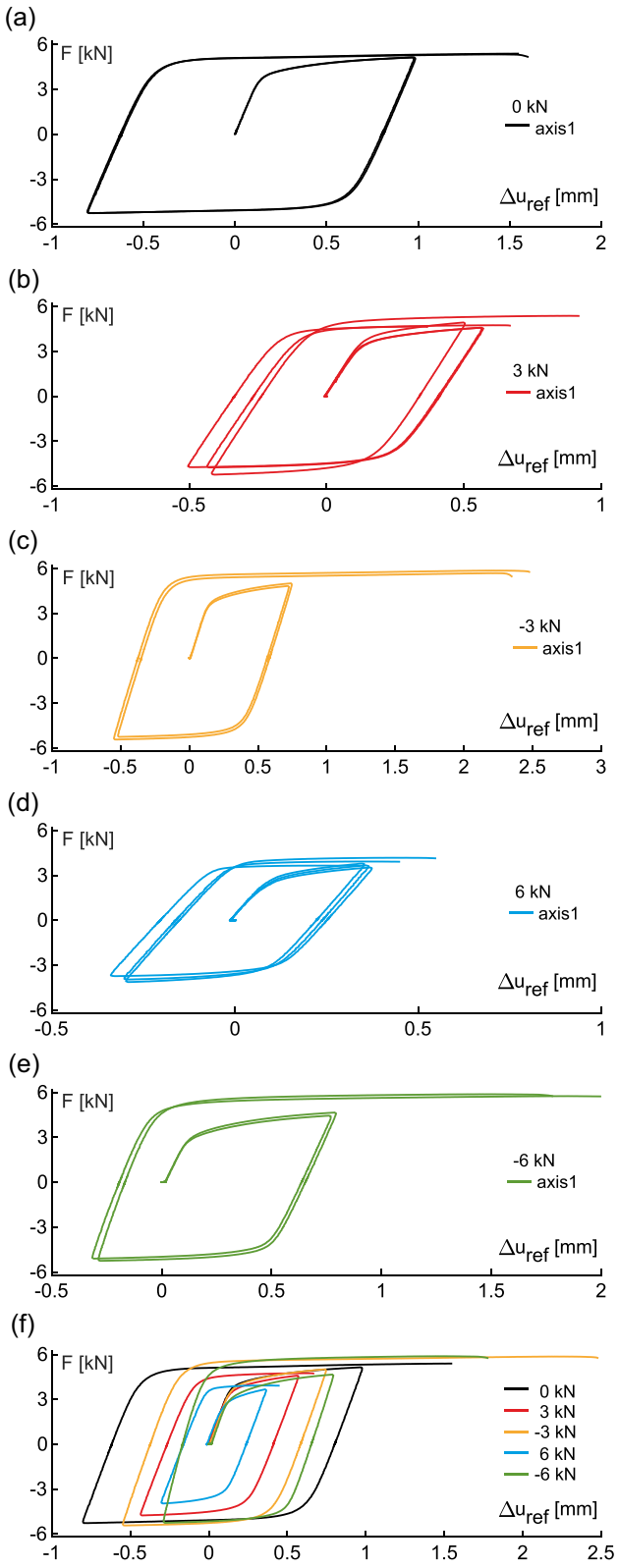

Fig. 8 The experimental force-displacement curves for cyclic loadings

Table 3 Relative displacement $\Delta u_{ref.2}$ in mm at characteristic points of the loading paths

Loading paths	AP	RP1	RP2	FP
0, mon	n.a.			0.21
3, mon	0.04			0.13
−3, mon	−0.04			−0.68
6, mon	0.08			0.34
−6, mon	−0.08			−1.11
0, cyc (TCT)	n.a.	0.06	−0.06	0.11
3, cyc (TCT)	0.03	0.07	0.26	0.25
−3, cyc (TCT)	−0.04	−0.18	−0.15	−0.77
6, cyc (TCT)	0.08	0.14	0.36	0.45
−6, cyc (TCT)	−0.07	−0.32	−0.36	−1.39

(b) and 6kN (d)), it is necessary to choose the displacements at RP1 and RP2 smaller with increasing tensile preload to avoid failure in the second half cycle and to allow a third half cycle. This can be taken as an indication of onset of ductile damage. Under compressive loading (−3 kN (c) and −6 kN (e)), RP1 could be selected at a larger relative displacement $\Delta u_{ref.1}$, whereas RP2 had to be selected earlier with as much displacement as possible until failure (FP). Under compressive loading, a significant increase in force at the onset of yielding is also observed in the third half cycle compared to the first half cycle. The slopes in the elastic region are similar for the first and second unloading and associated counterloading for load cases 0, 3, 6 and −3 kN, whereas −6 kN shows a stiffer behavior, see (f). The relative displacements at rupture of the cyclic tests are smaller compared to the corresponding tests with monotonic load increase (Fig. 7).

The comparison of the maximum relative displacement in axis 1 between the tests with monotonic load increase and those with cyclic load history shows some clear differences, see Figs. 7 and 8. Without preloading (0 kN), 2.3 mm are achieved with monotonic load increase and 1.7 mm with cyclic loading, i.e., a rather moderate difference. Under tensile preload there are significantly greater differences: at 3 kN 1.8 mm (mon) to 0.7 mm (cyc) and at 6 kN 1.2 mm (mon) to 0.4 mm (cyc). The differences become smaller under compression preloading with −3 kN: 2.9 mm (mon) to 2.5 mm (cyc) whereas at −6 kN the differences increase again moderately: 3.1 mm (mon) to 2.0 mm (cyc).

The strain fields on the specimen surface are detected and evaluated by the digital image correlation (DIC). Figure 9 shows the von Mises equivalent strain of the region of interest (ROI) for the five preloads under monotonic load increase at FP (left column) and under cyclic loading at RP1 (second column) and RP2 (third column) as well as just before fracture (FP, right column). The standard

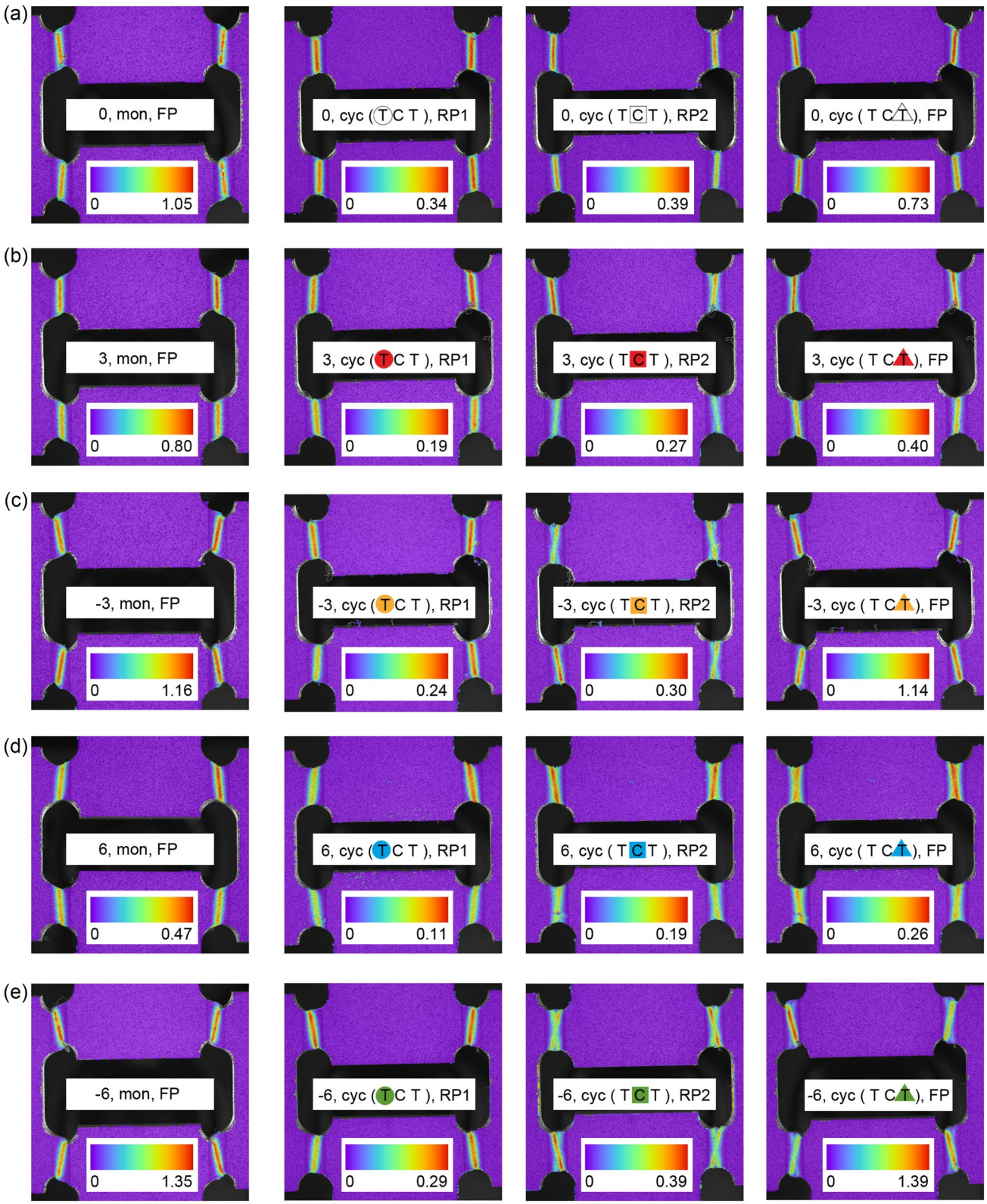

Fig. 9 Von-Mises equivalent strain for monotonic and cyclic loadings

deviation of the von Mises equivalent strain in the notch base reaches values of approximately 0.002; only for load cases with very high strains (−6 kN, Fig. 9(e), FP) values of 0.004 are recorded. Strain concentrations are found in each of the four notches. Under monotonic load increase (left column), it can be observed that the slope of the strain band as well as the maximum detected von Mises equivalent strain depend on the preload. Without preloading in axis 2 ((a), left column), the strain bands are inclined towards the center of the specimen and the maximum values of the strain are 1.05 at the FP. Under tensile preload, the strain band first forms parallel to the notches (3 kN, (b), left column) and inclines outward (6 kN, (d), left column) as tensile preload is further increased. With increasing tensile preload, the maximum measured strains decrease and reach only 0.47 at 6 kN. On the contrary, with increasing compressive superposition (−3 kN, (c), left column and −6 kN, (d), left column), the inclination of the strain band to the specimen center increases and the maximum values of the strain also increase up to 1.35 at −6kN. The inclination of the strain bands is directly related to the axis 1 loaded to the specimen outside. When loaded to the specimen center, it forms in the opposite direction, which comes into play when axis 1 is loaded cyclically in the second half cycle. In the first half cycle, strain bands with similar direction as under monotonic loading are formed, although these are even broader at significantly lower maximum values (RP1, second column). The strain bands at RP1 (second column) can also be understood as an earlier point in time of the corresponding test with monotonic load increase, since the tests are congruent up to this point. After load reversal in axis 1, the influences of the load direction become obvious at RP2, which is clearly reflected in the change of the inclination of the strain bands and leads to x-shaped increased strains. Between RP1 and RP2, there is only a moderate increase in maximum strain, since load reversal also causes strain to be reduced. In the third half-cycle up to the fracture, effects similar to those in the second half cycle can be observed. Clear differences between the prestrain at monotonic load increase and under cyclic loading are evident for 3 kN ((b) left and right column) and for −3 kN ((d) left and right column). After cyclic loading, less concentrated strains with a different slope are present. Overall, all four notches show very similar strain fields with a slight increase in individual notches towards failure (FP, right column). Specially under cyclic loading condition in some rare cases slipping effects at the specimen clamping is possible and can cause more significant differences in the present strain fields.

All tests in the series presented here were loaded until failure of the specimen. Figure 10 shows in the left column the fractured specimens after monotonic load increase and in the right column those after cyclic loading for the different preloads. In Fig. 10, it is clear that

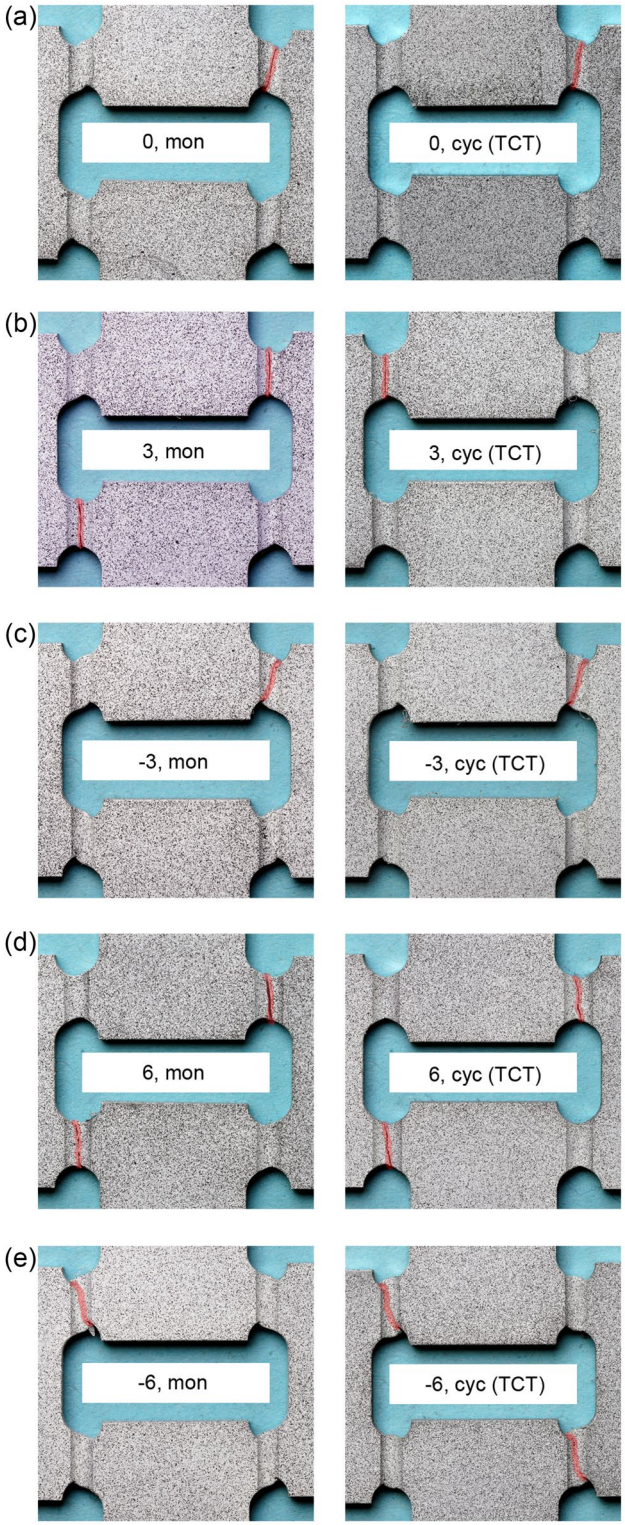

Fig. 10 Fractured specimens

towards the experiment end one or two notch regions fail, with the crack patterns highlighted in red. The crack patterns here reflect the strains determined shortly before fracture (cf. Fig. 9, left (monotonic load increase) and

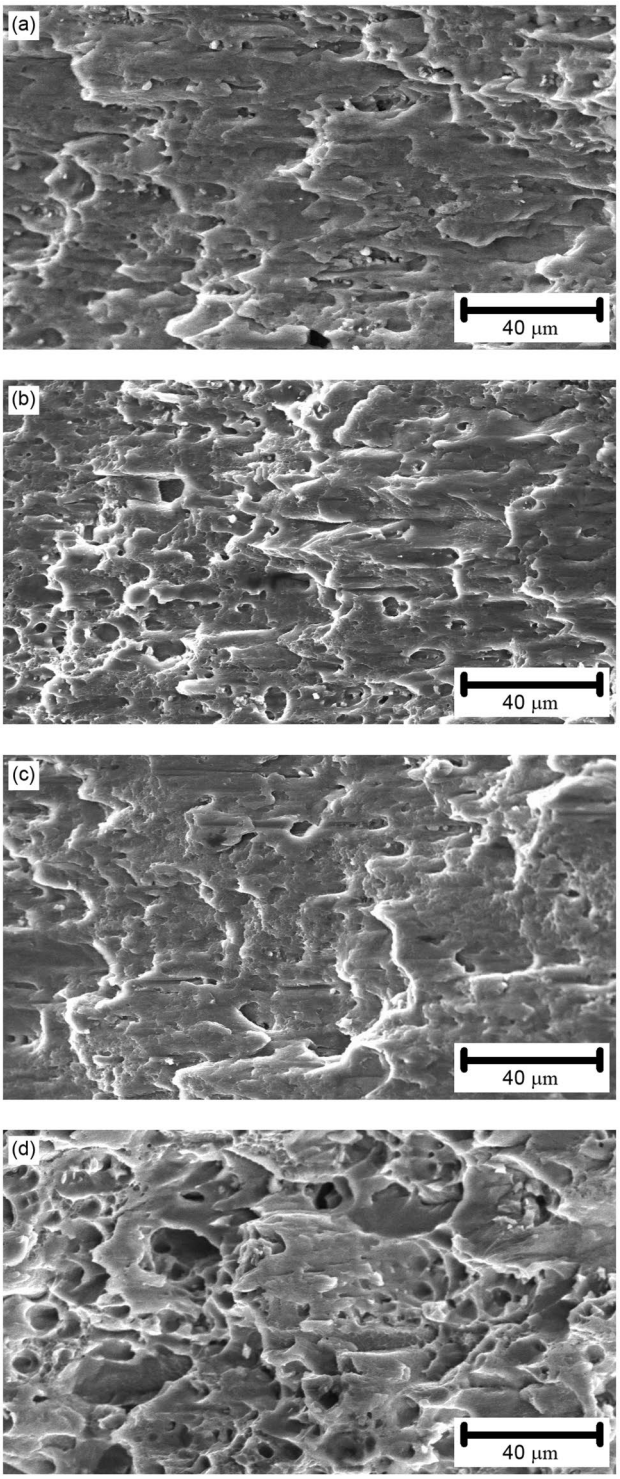

Fig. 11 SEM images of fracture surfaces monotonic loadings: (**a**) 0, (**b**) 3, (**c**) −3, (**d**) 6 kN

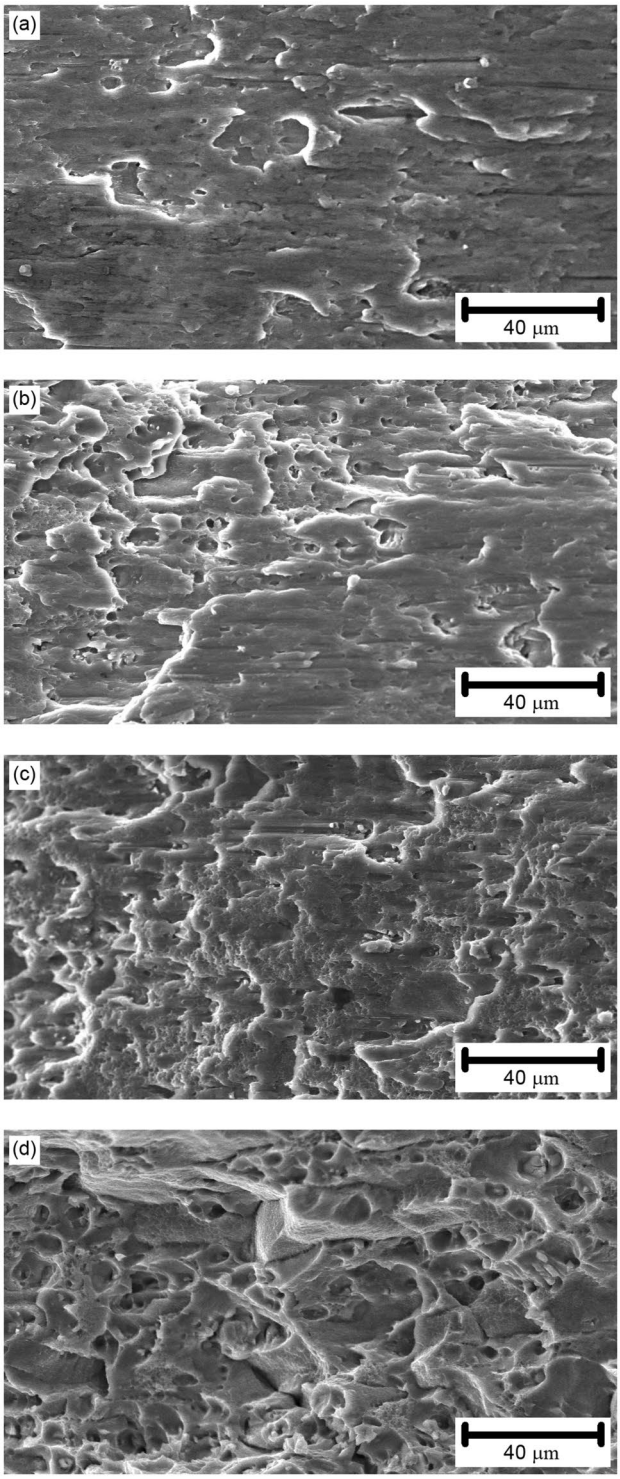

Fig. 12 SEM images of fracture surfaces cyclic loadings: (**a**) 0, (**b**) 3, (**c**) −3, (**d**) 6 kN

right column (cyclic load)) and the cracks occur along the maximum strains before fracture. Both the crack patterns and the deformed specimens after monotonic load increase and after cyclic loading at the same preload are very similar, although it is noticeable in the comparisons that the specimens after cyclic loading have a slightly smaller displacement in axis 1. The deformed and cracked specimens also reflect the preload in axis 2 very well,

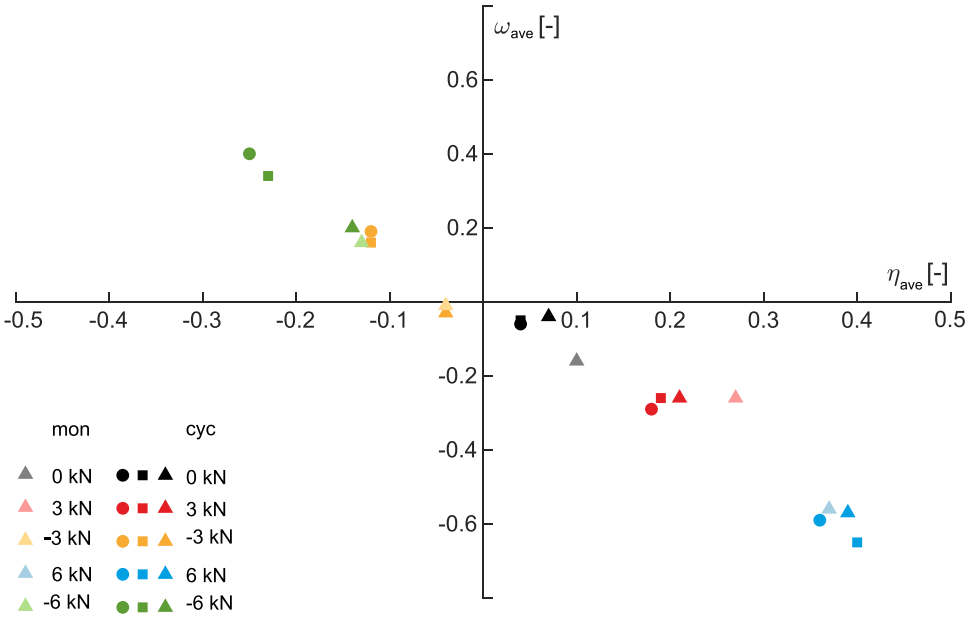

Fig. 13 Plots for the average values of the stress triaxiality η_{ave} and Lode parameter ω_{ave} under different loading paths

with an increase in the size of the notch areas (b and d) under tensile loading and their reduction (c and e) under compressive loading. It is also worth noting that after −6 kN preload, the crack was clearly visible after both monotonic and cyclic loading, but the cracked specimen parts could not be separated and consequently no analysis of the fracture surfaces by scanning electron microscopy (SEM) was possible for this load case.

For the other load cases under 0, 3, −3 and 6 kN preload, SEM images of the fracture surfaces were taken both after monotonic load application (Fig. 11) and after cyclic loading (Fig. 12), and a representative image in the center of the fracture surface was selected in each case. All fracture surfaces show clear signs of shear loading (axis 1) and the influence of preloading (axis 2) is also evident. Under compressive preload of −3kN, the fracture surfaces with monotonic load increase (Fig. 11(c)) and those after cyclic loading (Fig. 12(c)) show a similar surface of a shear fracture matching the stress triaxiality, see also Figs. 6(a), on this. At monotonic load increase (Fig. 11), the surface becomes progressively rougher ((a), 0 kN and (b), 3 kN) and under 6 kN preload (d), significant pore formation can be observed, indicating an onset of damage under tensile preload. The influence of preloading is not evident under cyclic loading (Fig. 12) under 0 kN (a) and 3 kN (b); the fracture surfaces show a similar fracture surface. Under 6 kN (d), however, as after monotonic load increase (Fig. 11(d)), significant pore formation can be seen and, in addition, microcracks perpendicular to the fracture surface appear, which can be explained by the cyclic loading history. Thus, the influence of the cyclic loading is clearly evident both below the different preloads and in comparison to the tests with monotonic load increase.

In addition to Fig. 6 where the distribution of the stress triaxiality η and Lode parameter ω in the notched cross

Table 4 The average stress triaxiality η_{ave} in the notched cross section under different loading paths

Loading paths	RP1	RP2	FP
0, mon			0.10
3, mon			0.27
−3, mon			−0.04
6, mon			0.37
−6, mon			−0.13
0, cyc (TCT)	0.04	0.04	0.07
3, cyc (TCT)	0.18	0.19	0.21
−3, cyc (TCT)	−0.12	−0.12	−0.04
6, cyc (TCT)	0.36	0.40	0.39
−6, cyc (TCT)	−0.25	−0.23	−0.14

Table 5 The average Lode parameter ω_{ave} in the notched cross section under different loading paths

Loading paths	RP1	RP2	FP
0, mon			−0.16
3, mon			−0.26
−3, mon			−0.01
6, mon			−0.56
−6, mon			0.16
0, cyc (TCT)	−0.06	−0.05	−0.04
3, cyc (TCT)	−0.29	−0.26	−0.26
−3, cyc (TCT)	0.19	0.16	−0.03
6, cyc (TCT)	−0.59	−0.65	−0.57
−6, cyc (TCT)	0.40	0.34	0.20

section are depicted the average value of the stress triaxiality and the Lode parameter over the notched cross section area, see Fig. 5, are defined as

$$\eta_{\text{ave}} = \frac{1}{S}\int_S \eta \, \mathrm{d}s \quad \text{and} \quad \omega_{\text{ave}} = \frac{1}{S}\int_S \omega \, \mathrm{d}s, \tag{12}$$

respectively, where S is the area of the corresponding cross section.

The sign of the shear stresses has no influence on the scalar values of the stress triaxiality (equation (8)) and the Lode parameter (equation (9)). Loading in axis 1 primarily causes shear stresses in the notch regions of the specimen. Equation (12) can be used to determine the average stress triaxiality η_{ave} and average Lode parameters at the load reversal points (RP1 and RP2) and just before fracture (FP) based on the numerical simulations performed. These values are shown in Fig. 13 in the η_{ave}-ω_{ave} plane graphically and listed in the Tables 4 and 5. The values of the tests with the same preload in axis 2 under monotonic and under cyclic loading are very close to each other, whereas under compressive preload at the reversal points (RP1 and RP2) there are somewhat larger deviations, see Fig. 13. Furthermore, the determined points are located approximately on a straight line in the η_{ave}-ω_{ave} plane. The presented test results show a clear influence of the cyclic loading on the deformation and damage behavior, here the stress triaxiality and the Lode parameter remain nearly invariant during the experiments.

Conclusions

The new ideas, experimental techniques and results presented in this paper indicate the reliable starting point to investigate the ductile material behavior including damage and fracture under cyclic loading and consideration of a big variety of stress states. Furthermore, these results can be used to quantify the history dependent inelastic, namely plastic and damage, behavior of ductile sheet metals. The fractured specimens reveal all the characteristics of ductile failure, i.e., in particular, no evidence of fatigue failure could be detected. The new conclusions and findings from this paper can be summarized as follows:

- The newly introduced specimen allows tensile and compressive loads in both axes. This enables cyclic load paths in both axes, whereby cyclic shear loads under tension and compression superposition are considered in the series presented here. In the future, this specimen geometry can be used to investigate a wide variety of cyclic load histories under a wide range of stress conditions.
- The newly introduced downholder allows larger compressive loads to be applied without buckling. The special design further allows the use of digital image correlation (DIC) in a restricted working space.
- The experimental series indicates the influence of compressive and tensile preloading superimposed to cyclic shear loading on the maximum displacement in relation to monotonic loading. Tensile preloads lead to significantly lower maximum displacements at fracture and with compressive preloads there is little influence of cyclic load history on the maximum displacement.
- For the cyclic loading specifically chosen here, the stress triaxiality and the Lode paramenter remain approximately constant during the load cycles. However, the scanning electron micrographs of the fracture surfaces show a clear influence of the cyclic loading on the deformation and damage behavior.
- Through the use of a biaxial test specimen, specific and measurable loads can be applied in axis 2 and, thus, the shear load from axis 1 can be targeted with tension or compression superimposed.

Funding Open Access funding enabled and organized by Projekt DEAL. The project has been funded by the Deutsche Forschungsgemeinshaft (DFG, German Research Foundation) - project number 322157331, this financial support is gratefully acknowledged.

Declarations

Conflict of Interest The authors declare that they have no conflict of interest.

Open Access This article is licensed under a Creative Commons Attribution 4.0 International License, which permits use, sharing, adaptation, distribution and reproduction in any medium or format, as long as you give appropriate credit to the original author(s) and the source, provide a link to the Creative Commons licence, and indicate if changes were made. The images or other third party material in this article are included in the article's Creative Commons licence, unless indicated otherwise in a credit line to the material. If material is not included in the article's Creative Commons licence and your intended use is not permitted by statutory regulation or exceeds the permitted use, you will need to obtain permission directly from the copyright holder. To view a copy of this licence, visit http://creativecommons.org/licenses/by/4.0/.

References

1. Tutyshkin N, Müller WH, Wille R, Zapara M (2014) Strain-induced damage of metals under large plastic deformation: theoretical framework and experiments. Int J Plast 59:133–151
2. Chait R (1972) Factors influencing the strength differential of high strength steels. Metall Mater Trans B 3(2):369–375
3. Holmen JK, Frodal BH, Hopperstad OS, Børvik T (2017) Strength differential effect in age hardened aluminum alloys. Int J Plast 99:144–161
4. Spitzig WA, Richmond O (1984) The effect of pressure on the flow stress of metals. Acta Metall 32(3):457–463
5. Gomez J, Basaran C (2006) Damage mechanics constitutive model for Pb/Sn solder joints incorporating nonlinear kinematic hardening and rate dependent effects using a return mapping integration

algorithm. Mechanics of Materials: An International Journal 38(7):585–598
6. Park T, Chung K (2012) Non-associated flow rule with symmetric stiffness modulus for isotropic-kinematic hardening and its application for earing in circular cup drawing. Int J Solids Struct 49(25):3582–3593
7. Taherizadeh A, Green DE, Ghaei A, Yoon JW (2010) A non-associated constitutive model with mixed iso-kinematic hardening for finite element simulation of sheet metal forming. Int J Plast 26(2):288–309
8. Wei Z, Zistl M, Gerke S, Brünig M (2022) Analysis of ductile damage evolution and failure mechanisms due to reverse loading conditions for the aluminum alloy EN-AW 6082–T6. Proc Appl Math Mech 22
9. Bao Y, Wierzbicki T (2004) On fracture locus in the equivalent strain and stress triaxiality space. Int J Mech Sci 46(1):81–98
10. Brünig M, Chyra O, Albrecht D, Driemeier L, Alves M (2008) A ductile damage criterion at various stress triaxialities. Int J Plast 24(10):1731–1755
11. Brünig M, Gerke S, Zistl M (2019) Experiments and numerical simulations with the H-specimen on damage and fracture of ductile metals under non-proportional loading paths. Eng Fract Mech 217
12. Gerke S, Zistl M, Bhardwaj A, Brünig M (2019) Experiments with the X0-specimen on the effect of non-proportional loading paths on damage and fracture mechanisms in aluminum alloys. Int J Solids Struct 163:157–169
13. Wei Z, Zistl M, Gerke S, Brünig M (2022) Analysis of ductile damage and fracture under reverse loading. Int J Mech Sci 228:107476
14. Bai Y, Wierzbicki T (2008) A new model of metal plasticity and fracture with pressure and Lode dependence. Int J Plast 24(6):1071–1096
15. Bonora N, Gentile D, Pirondi A, Newaz G (2005) Ductile damage evolution under triaxial state of stress: theory and experiments. Int J Plast 21(5):981–1007
16. Roth CC, Mohr D (2016) Ductile fracture experiments with locally proportional loading histories. Int J Plast 79:328–354
17. Miyauchi K (1984) Proposal of a planar simple shear test in sheet metals. Sci Pap Inst Phys Chem Res (Jpn) 78(3):27–40
18. Yin Q, Soyarslan C, Isik K, Tekkaya AE (2015) A grooved in-plane torsion test for the investigation of shear fracture in sheet materials. Int J Solids Struct 66(66):121–132
19. Brosius A, Yin Q, Güner A, Tekkaya AE (2011) A new shear test for sheet metal characterization. Steel Res Int 82(4):323–328
20. Dunand M, Mohr D (2011) On the predictive capabilities of the shear modified Gurson and the modified Mohr-Coulomb fracture models over a wide range of stress triaxialities and Lode angles. J Mech Phys Solids 59(7):1374–1394
21. Dunand M, Mohr D (2011) Optimized butterfly specimen for the fracture testing of sheet materials under combined normal and shear loading. Eng Fract Mech 78(17):2919–2934
22. Arcan M, Hashin Z, Voloshin A (1978) A method to produce uniform plane-stress states with applications to fiber-reinforced materials. Exp Mech 18(4):141–146
23. Alves LM, Nielsen CV, Martins PAF (2011) Revisiting the fundamentals and capabilities of the stack compression test. Exp Mech 51(9):1565–1572
24. Farahnak P, Urbanek M, Rund M, Džugan J, Gerke S, Brünig M (2019) New approach for determination of strain rate sensitivity of mild steel DC01 under stack compression and uniaxial tensile tests. In: Oñate E (ed) Proceedings of COMPLAS 2019 : CIMNE Barcelona. pp 489–498
25. Pawelski O (1967) Über das Stauchen von Hohlzylindern und seine Eignung zur Bestimmung der Formänderungsfestigkeit dünner Bleche. Archiv für das Eisenhüttenwesen 38(6):437–442
26. Cao J, Lee W, Cheng HS, Seniw M, Wang HP, Chung K (2009) Experimental and numerical investigation of combined isotropic-kinematic hardening behavior of sheet metals. Int J Plast 25(5):942–972
27. Ramberg W, Miller JA (1946) Determination and presentation of compressive stress-strain data for thin sheet metal. Journal of the Aeronautical Sciences 13(11):569–580
28. Yoshida F, Uemori T, Fujiwara K (2002) Elastic-plastic behavior of steel sheets under in-plane cyclic tension-compression at large strain. Int J Plast 18(5–6):633–659
29. Gerke S, Schmidt M, Dirian M, Brünig M (2018) Damage and fracture of ductile sheet metals: experiments and numerical simulations with new biaxial specimens. In: Altenbach F, Jablonski F, Müller WH, Naumenko K, Schneider P (eds) Advances in mechanics of materials and structural analysis, vol 80. Springer International Publishing, pp 99–116. https://doi.org/10.1007/978-3-319-70563-7_5
30. Kuwabara T (2007) Advances in experiments on metal sheets and tubes in support of constitutive modeling and forming simulations. Int J Plast 23(3):385–419
31. Gerke S, Adulyasak P, Brünig M (2017) New biaxially loaded specimens for the analysis of damage and fracture in sheet metals. Int J Solids Struct 110–111:209–218
32. Bouchard PO, Bourgeon L, Lachapèle H, Maire E, Verdu C, Forestier R, Logé RE (2008) On the influence of particle distribution and reverse loading on damage mechanisms of ductile steels. Mater Sci Eng, A 496(1–2):223–233
33. Cortese L, Nalli F, Rossi M (2016) A nonlinear model for ductile damage accumulation under multiaxial non-proportional loading conditions. Int J Plast 85:77–92
34. Korkolis YP, Kyriakides S (2009) Path-dependent failure of inflated aluminum tubes. Int J Plast 25(11):2059–2080
35. Kim KH, Yin JJ (1997) Evolution of anisotropy under plane stress. J Mech Phys Solids 45(5):841–851
36. Tarigopula V, Hopperstad OS, Langseth M, Clausen AH (2008) Elastic-plastic behaviour of dual-phase, high-strength steel under strain-path changes. Eur J Mech A Solids 27(5):764–782
37. Brünig M (2003) An anisotropic ductile damage model based on irreversible thermodynamics. Int J Plast 19(10):1679–1713
38. Hirt JP, Cohen M (1970) On the strength-differential phenomenon in hardened steel. Metall Mater Trans B Process Metall Mater Process Sci 1: 3–8
39. Brünig M, Gerke S, Hagenbrock V (2013) Micro-mechanical studies on the effect of the stress triaxiality and the Lode parameter on ductile damage. Int J Plast 50:49–65
40. Wei ZM, Gerke S, Brünig M (2023) Characterization of ductile damage and fracture behavior under shear reverse loading conditions. Proc Appl Math Mech 23:e202300031
41. Wei ZM, Gerke S, Brünig M (2023) Damage and fracture behavior under non-proportional biaxial reverse loading in ductile metals: experiments and material modeling. Int J Plast 171:103774
42. Wei ZM, Gerke S, Brünig M (2024) Numerical analysis of non-proportional biaxial reverse experiments with a two-surface anisotropic cyclic plasticity-damage approach. Comput Methods Appl Mech Eng 419:1116630
43. Brünig M, Zistl M, Gerke S (2021) Numerical analysis of experiments on damage and fracture behavior of differently preloaded aluminum alloy specimens. Metals 11(3):381
44. Jones EMC, Iadicola MA (eds) (2018) International digital image correlation society: a good practices guide for digital image correlation. https://doi.org/10.32720/idics/gpg.ed1/print.format

Publisher's Note Springer Nature remains neutral with regard to jurisdictional claims in published maps and institutional affiliations.